

Octahedral rotations and defect-driven metallicity at the (001) surface of CaTiO₃Manali Vivek,¹ Jacek Goniakowski,² Andrés Santander-Syro ,³ and Marc Gabay⁴¹Université Paris-Saclay, CNRS, Laboratoire de Physique des Solides, Orsay 91405, France²CNRS, Sorbonne Université, Institut des NanoSciences de Paris, UMR 7588, 4 Place Jussieu, F-75005 Paris, France³Université Paris-Saclay, CNRS, Institut des Sciences Moléculaires d'Orsay, 91405 Orsay, France⁴Université Paris-Saclay, CNRS, Laboratoire de Physique des Solides, Orsay 91405, France (Received 28 June 2022; revised 10 November 2022; accepted 21 December 2022; published 3 January 2023)

Defect-free CaTiO₃ is a band insulator, but angle-resolved photoemission spectroscopy experiments have demonstrated the existence of a nanometer-thin two-dimensional electron system (2DES) at the (001)-oriented surface of this compound. Our *ab initio* study finds that while oxygen defects are the driving mechanism for the metallicity, tiltings and rotations of the oxygen octahedra significantly impact the electronic structure of the 2DES and its response to externally applied strain deformations. The low-energy conduction subbands have a mixed t_{2g} - e_g orbital character close to the center of the Brillouin zone. Good agreement with the experimental spectra is found for TiO₂ surface divacancy configurations.

DOI: [10.1103/PhysRevB.107.045101](https://doi.org/10.1103/PhysRevB.107.045101)**I. INTRODUCTION**

Multifunctional materials have been identified as key components for developing low-power technologies. In this respect, transition-metal oxides have been the focus of renewed theoretical and experimental attention as they possess tunable properties of ferroelectricity, magnetism, colossal magnetoresistance, multiferroicity, and superconductivity originating from the delicate interplay of structural, electronic, and magnetic correlations [1,2]. Novel functionalities can also be imparted to heterostructures where at least one of the constitutive compounds is a transition-metal oxide perovskite [3–6]. A two-dimensional metallic state (2DES) was evidenced near the interface of the wide-band-gap insulators LaAlO₃ and SrTiO₃ (STO), which also harbors superconductivity [7–9] and a large tunable Rashba spin-orbit coupling [10], creating promising opportunities for spintronics [11,12]. Additionally, angle-resolved photoemission spectroscopy (ARPES) measurements of bare or capped surfaces of several ATiO₃ perovskites ($A = \text{Sr, Ba, Ca}$) and KTaO₃ have uncovered a confined 2DES [13–15]; in the case of STO, indications of magnetism were proposed and the theoretical prediction of a topological state was made [16–18]. For *a priori* nonpolar materials, such as STO and CaTiO₃ (CTO), experimental evidence suggests that oxygen vacancies positioned near the surface provide the conduction-band carriers forming the metallic state [19–22].

Bulk CTO is an insulator with a band gap of 3.5 eV [23]. Below 1300 K, large rotations and tiltings of the oxygen octahedra force CTO to become orthorhombic [24] with rotation ($\phi = 9^\circ$) and tilt ($\theta = 12^\circ$) angles [25]. ARPES [21,22] on the oxygen-deficient UHV clean (001) surface reveals an in-gap state around 1.3 eV below the Fermi energy E_F and three occupied bands, constitutive of a 2DES. The first and third bands have a dominant d_{xy} character close to Γ , the center of

the Brillouin zone (BZ). The second band is of mixed $d_{xz/yz}$ character in the vicinity of Γ and the shape of the Fermi surface suggests a significant hybridization between the heavy orbitals close to Γ . This indicates that rotations couple to other degrees of freedom, thus promoting an even broader variety of ground states and providing extra handles to tune the flow of charge.

In order to set these considerations on firmer ground, we performed a density functional theory (DFT) study of the confined metallic bands and in-gap state at the surface of CTO, in the presence of oxygen defects. We explicitly allow rotations of the Ti-O octahedra in our calculations. While these has been previously included in *ab initio* computations of bulk CTO electronic spectra, DFT studies of CTO surfaces have been restricted to a cubic structure [21,26,27]. Rotations of the octahedra introduce additional sources of relaxations, which make the computation far more involved than in the simpler case of STO. Our calculations underscore the impact of these distortions on the surface characteristics, affecting the band structure of CTO. For STO, the main features of the experimental spectra were captured in DFT computations of asymmetric slabs with subsurface apical oxygen divacancies positioned at the SrO termination. We explored various configurations of single vacancies and divacancies, and considered different values of U . For CTO, a fair agreement with the experimentally determined electronic structure is found when we introduce horizontal surface divacancies at the TiO₂ termination and set $U = 4.5$ eV and $J = 0.64$ eV. A metallic state is observed, as well as a localized in-gap level positioned approximately 1 eV below E_F . The impact of rotations is evidenced by the mixing of all three t_{2g} orbitals at the conduction-band minimum and a sizable hybridization between e_g and t_{2g} orbitals in the conduction-band states, causing a weaker quantum confinement strength. As a result, compared to STO where such mixing is not significant, the

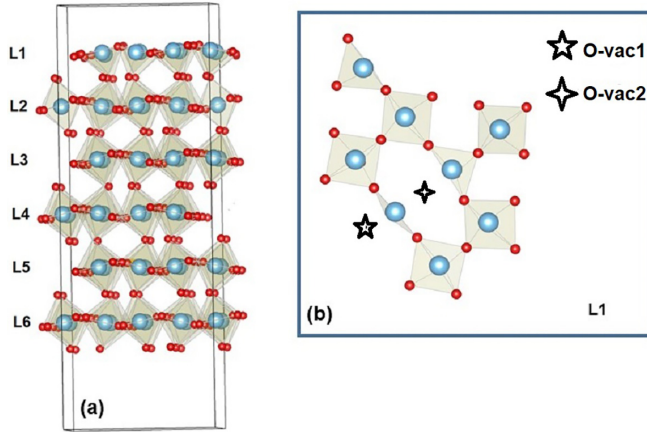


FIG. 1. (a) Stoichiometric $2 \times 2 \times 6$ slab in the orthorhombic lattice basis composed of six CaTiO_3 blocks, each of which consists of one CaO and one TiO_2 layer. The TiO_2 atomic layers are labeled L_i . The index i ($i = 1-6$) is the layer number. We only show Ti atoms (blue) and O atoms (red). (b) When one (O-vac1) and two (O-vac1, O-vac2) oxygen vacancies are created at the TiO_2 termination (L1), they are placed along the (pseudocubic) x Ti-O-Ti bond direction.

lowest-energy band lies much closer to E_F and the mass of the carriers is larger.

II. COMPUTATIONAL METHOD

All DFT calculations were performed with the Vienna Ab-initio Simulation Package (VASP) [28,29]. The interaction of valence electrons with ionic cores was described within the projector augmented wave (PAW) method [30,31] and the Kohn-Sham orbitals were developed on a plane-wave basis set. Standard calcium and titanium (including $3p$ electrons in the valence band), and soft oxygen pseudopotentials (energy cutoff of 300 eV) provided with VASP, were used. The applicability of the soft oxygen pseudopotential was validated with results obtained with a standard oxygen pseudopotential (energy cutoff of 400 eV); see the Supplemental Material in Ref. [21]. In order to better capture the main features of the electronic structure, in particular the position and character of the gap edges, the gradient-corrected exchange-correlation functional (PW91) [32] was employed within the DFT+ U approach proposed by Dudarev [33]. Having fixed the J value to 0.64 eV, we have systematically tested several values of the U parameter in the range 2.5–5.5 eV, and found that the best agreement with the experimental results was obtained for $U = 4.5$ eV, close to the value previously reported for STO [34,35]. Since there are no experimental indications of magnetism, all of our calculations are non-spin-polarized.

Oxygen vacancies were placed at either the TiO_2 or CaO termination of a (001)-oriented asymmetric CTO slab (Fig. 1) and the positions of all atoms were fully relaxed along the x , y , and z directions until all forces became smaller than 0.01 eV/Å. In order to avoid any bias with respect to the spatial localization of the 2DES, a thick slab, composed of six CaTiO_3 units (12 atomic layers), was used. Slabs were separated by more than 10 Å of vacuum and dipole corrections were applied to further reduce the spurious interactions

between periodic images in the direction perpendicular to the surface. The same (2×2) -CTO(001) surface unit cell was systematically used in all calculations on perfect and O-deficient surfaces. It corresponds to a $(2\sqrt{2} \times 2\sqrt{2})$ surface cell in the pseudocubic basis (with the x and y axes oriented along the Ti-O-Ti bond directions) to which we will refer in the following in order to compare our data to the ARPES spectra. We note that a single oxygen defect in such a surface unit cell results in a 2DES density of about 0.01 e/Å², very close to the experimental estimation [21].

The first BZ of the surface cell was sampled on a dense Γ -centered (6×6) Monkhorst-Pack grid [36]. Considering the metallic character of the O-deficient surfaces, the convergence with respect to the k -point sampling was further improved by applying a Gaussian smearing of 0.1 eV. For band plotting, eigenvalues and eigenvectors at 20 k points along the $\Gamma - X$ and $\Gamma - M$ directions were evaluated in dedicated non-self-consistent runs, with the electron densities obtained in prior fully self-consistent calculations. No further band folding/unfolding was applied. For each band and at each k point, the orbital character of the wave functions was estimated with the help of PAW projector functions.

III. RESULTS

A. Defect-free slab

Towards the center of the slab, considered to be representative of bulk CTO, the values of the rotation, tilt, and lattice parameters are $\phi = 9.8^\circ$, $\theta = 13.6^\circ$, $a = 5.42$ Å, $b = 5.54$ Å, and $c = 7.74$ Å. These values compare well with those reported in the Supplemental Material, Table S-1, of [21]. At the TiO_2 termination, however, ϕ is nearly 30% smaller, the apical Ti – O bond length is 1.9 Å (1.99 Å in layers L3 and L4), and a reduction of the band gap of about 1 eV is seen in the projected density of states, caused by the upward shift in energy of the valence band at the (TiO_2) L1 layer as compared to its position at the center of the slab (Fig. 2).

These deviations stem from the fact that at the surface, octahedra are missing an apical O and the corresponding bond. This causes distortions of the bond lengths and angles and also entails weaker electronic cohesion, primarily affecting the (oxygen) valence-band states. Note that the reduction of the gap size is also seen at the STO and BTO surfaces with very similar magnitudes [37,38], suggesting a rather modest influence of the rotations and tilts of the octahedra for this particular effect.

B. Oxygen vacancies

Guided by existing *ab initio* studies of STO [39], we consider single vacancies and divacancies in the direct vicinity of the TiO_2 or CaO end layers, since experiments suggest that the cleaved surface of CTO, which is predominantly of TiO_2 character, also exhibits patches of CaO ordering.

1. Vacancies at the CaO termination

Our DFT calculations indicate that a single oxygen vacancy at the CaO termination results in an insulating state. By contrast, when divacancies are present (Fig. 3), the band structure reveals occupied states below E_F as well as an in-gap

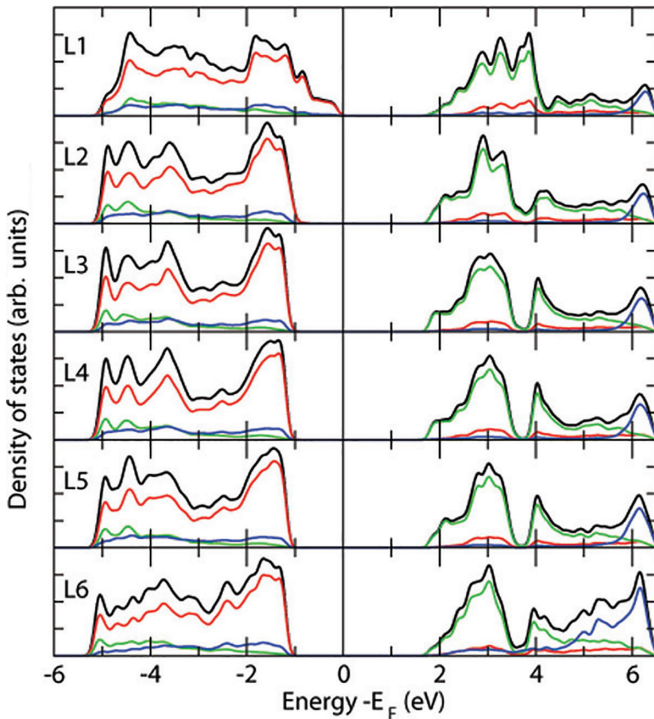


FIG. 2. Layer projected density of states (DOS). Contributions from the O (red), Ti (green), and Ca (blue) atoms are shown as well as the total DOS of each layer (black).

state. For the configurations that we considered, the localized state has an energy of the order of 1.3 eV with respect to E_F (inset of Fig. 3) and is of e_g character. Figure 3(a) corresponds to the case of two oxygen vacancies at the CaO surface. Near Γ , the orbital character of the occupied conduction bands is predominantly of d_{xy} character and the dispersion of the lowest-energy band at E_F shows a strong anisotropy. Figure 3(b) displays the spectrum for the case of an apical divacancy in one of the subsurface (layer L6) Ti-O octahedra. The lowest occupied conduction band disperses very weakly across the BZ and, in the vicinity of Γ , the orbital character of the three occupied bands is dominantly d_{xy} ($\sim 70\%$) plus a $\sim 20\%$ admixture of d_{xz} or d_{yz} components. For either case, the DFT band structure of the occupied states does not match its experimental counterpart, at variance with STO where apical divacancies at the SrO end led to a fair agreement with the ARPES spectra.

2. Vacancies at the TiO_2 termination

Figure 4(a) shows that a single oxygen vacancy at the TiO_2 layer L1 gives rise to a 2DES where the orbital character of the eigenfunctions is consistent with ARPES, but, as seen in the inset, no in-gap state is present. This suggests that the electrostatic potential associated with the defect is not strong enough to localize carriers in its vicinity. A horizontal divacancy at the TiO_2 surface, by contrast, gives a band structure in fair agreement with experiments [Fig. 4(b)] when $U = 4.5$ eV and $J = 0.64$ eV. The localized state, located approximately 1 eV below E_F , is of $d_{x^2-y^2}$ character and hosts two electrons. Similar to what is observed in several perovskite oxide 2DES near the BZ center, the lowest conduction band has a dominant d_{xy}

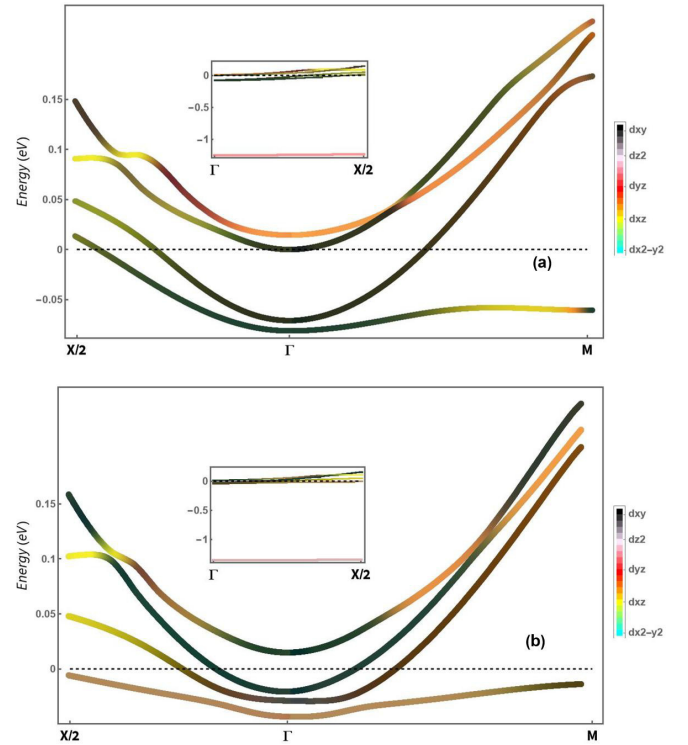


FIG. 3. Energy dispersion of conduction-band states along a X - Γ - M path when divacancies are present close to the CaO termination: (a) a slab with a horizontal divacancy at the CaO surface and (b) a slab with an apical divacancy in one of the (L6 layer) TiO_2 octahedra. Energies are measured relative to E_F , which is conventionally set to zero (dashed line). At every k point, the dominant orbital character of a given band eigenstate is indicated by a color which is assigned to each of the five d orbitals (see color chart). For instance, black corresponds to d_{xy} , orange to comparable weights of d_{xz} and d_{yz} . Insets in (a) and (b) display the e_g character in-gap state located ~ 1.3 eV below E_F .

character, as it is less affected by the quantum confinement. However, for CTO, there is also a $\sim 35\%$ admixture of d_{yz} orbital (when the divacancy is along x).

Near Γ , the second energy eigenstate is an approximately equal weight combination of d_{xz} , d_{yz} , and d_{z^2} orbitals where electrons occupy the first five layers from the top surface. As k increases, the orbital nature of this band evolves to a pure d_{xz} or d_{yz} character. The next band is mainly of d_{xy} character plus a $\sim 15\%$ $d_{x^2-y^2}$ mix. The bottom of the lowest conduction band is positioned approximately 100 meV below E_F . The experimental value is around 160 meV [21]. This is significantly less than what was found for STO [39], which indicates that confinement is much weaker in the case of CTO. A parabolic fit near Γ yields effective masses $m_1 = 0.9 m_e$ and $m_2 = 2.0 m_e$ along ΓX for the lowest and second-lowest bands, respectively (m_e is the bare electron mass). Experimental estimates of the masses gave $m_1 = 1.1 m_e$ and $m_2 = 2.7 m_e$; we comment on this below. Figure 5 overlays the DFT dispersion on top of the ARPES spectrum. We notice a fair agreement between the two sets of band structures. As mentioned in the previous paragraph, the DFT determined

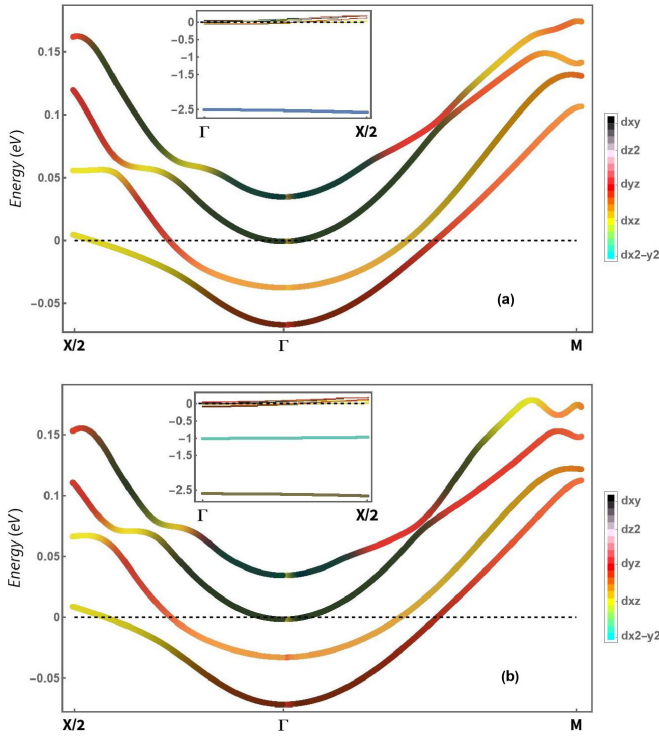


FIG. 4. Energy dispersion of conduction-band states along a X - Γ - M path when vacancies are present at the TiO_2 termination (see Fig. 1): (a) a slab with a single vacancy and (b) a slab with a horizontal divacancy in layer L1. Energies are measured relatively to E_F , which is conventionally set to zero (dashed line). At every k point, the dominant orbital character of a given band eigenstate is indicated by a color which is assigned to each of the five d orbitals (see color chart). Insets in (a) and (b) span the energy range between the last valence band and the conduction band. In (b), an in-gap state of $d_{x^2-y^2}$ character is located ~ 1 eV below E_F .

Γ -point energy of the lowest conduction band is 40% higher than its ARPES counterpart.

A map of the carrier occupation at each TiO_2 layer (Fig. 6) shows that the wave function corresponding to the in-gap state resides at the surface layer L1. In fact, it peaks at the Ti atom between the two vacancies (Fig. 1). Furthermore, at Γ , the d_{xy} component of the lowest three eigenstates is largest at layer L2 while the d_{yz} part spreads over the first five layers. Overall, the 2DES electronic density exhibits a large maximum at layer L2 (Fig. 7), indicative of a subsurface confinement.

The scope of our study is dictated by several experimental and computational considerations. ARPES probes extended regions of the sample boundary which may exhibit local reconstructions, steps, and host a broad range of vacancy configurations. Bond lengths and angles in the material, as well as Coulomb contributions to the energy, all show significant deviations from their values in the bulk. For CTO, rotations of the octahedra add an extra element of complexity. Also, given the known limitations of *ab initio* calculations, one should not expect to achieve a fully quantitative match between DFT and ARPES spectra. Hence, we focused on a determination of the band structure that yields a fair agreement between DFT and ARPES in two respects, i.e., the positions of the in-gap state and conduction bands relative to the Fermi energy, on

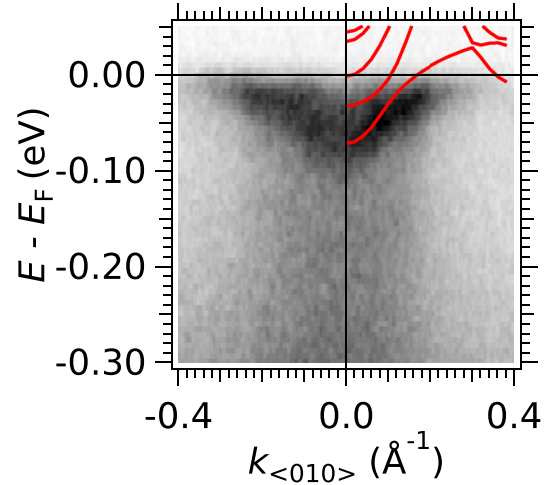


FIG. 5. The DFT-determined conduction-band structure for a divacancy at layer L1 (in red) is overlaid on top of the ARPES spectrum of Ref. [21].

the one hand, and the orbital weights of the corresponding eigenstates, on the other hand. The DFT values of the lattice parameters and rotation angles at the center of the slab were considered to be bulklike (see first paragraph of Sec. III). They are larger than the experimental ones (see Supplemental Material, Table S-1, of [21]), suggesting an underestimated degree of metallicity for the 2DES. We note that our *ab initio* calculations yield a value of the energy at the bottom of the lowest conduction band, relative to E_F that is approximately 40% less than that extracted from the ARPES spectra (Fig. 5), consistent with a weaker metallic trend. Also, larger rotations favor a stronger mixing between the t_{2g} and e_g orbitals. We remarked that the conduction bands with dominant d_{xy} character also include other t_{2g} or e_g orbital components. Similarly, the wave function of the second-lowest conduction band, which consists of an equal weight of d_{xz} and d_{yz} components, also features a sizable d_{z^2} part. Analysis of the ARPES spectra [21] led to the conclusion that while e_g and t_{2g} orbitals do

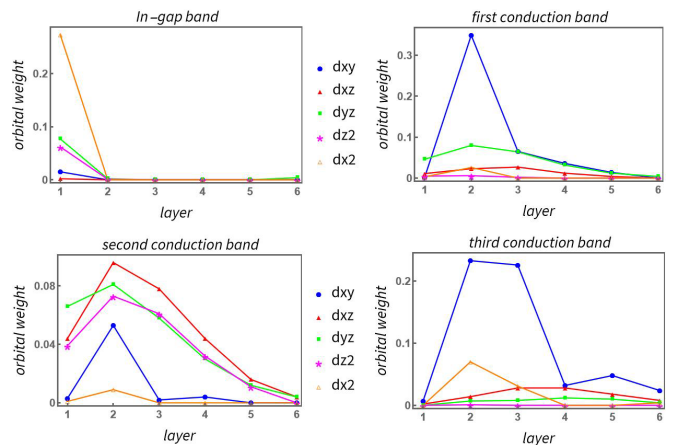


FIG. 6. The d -orbital weights at Γ in a slab with a divacancy. For a given band (we show the in-gap and three lowest in energy), we extract the weights of the five d -orbital components of the eigenfunction, projected onto each of the six TiO_2 layers.

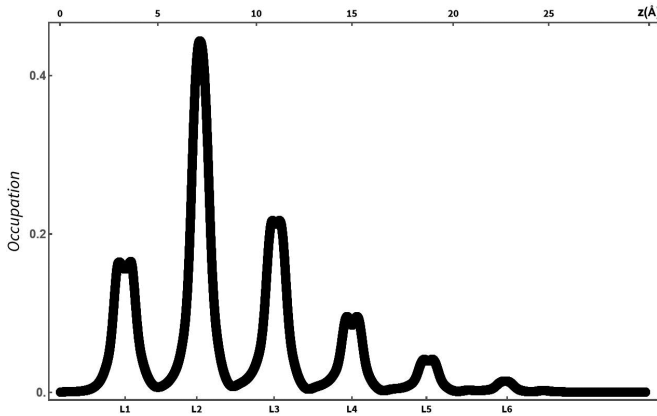


FIG. 7. The layer-resolved electronic density vs the layer number. A significant fraction of 2DES is located at the subsurface layer L2.

mix, the weight of the former in the eigenstates is smaller than what DFT finds. Next, we assess the dependence of the above markers on the structural parameters of the bulk. To this end, we use two knobs. One is the value of the Hubbard U that is chosen for the calculations. The other is the strength of a biaxial in-plane strain, which modifies the corresponding lattice parameters.

3. Role of Coulomb interactions and strain

Experimental and theoretical investigations of transition-metal oxides [40–42] suggest that the value of U that pertains to Ti compounds is between 2 and 5 eV, and accordingly we explored the evolution of the in-gap and conduction-band states when we choose the value of the Hubbard U in that range. The top panel of Fig. 8 shows the variation of the energy at Γ of the lowest conduction states versus U . Relative to E_F , an increase in U results (in absolute value) in a decrease in the confinement energy, which we interpret as indicative of a decreasing degree of metallicity.

The weight of the d_{xy} component of the low-energy conduction-band eigenstates is only nonzero at layers L2 and L3, while that of the d_{xz} , d_{yz} , and d_{z^2} components is distributed across the entire slab, as seen in Fig. 6. We infer from this observation that U causes a larger rise in energy for bands with dominant d_{xy} or $d_{x^2-y^2}$ character, which are more localized than for those with d_{xz} , d_{yz} , and d_{z^2} dominant character, which are more extended. This helps explain why, between Γ and E_F , the eigenstate consisting of a combination of d_{xz} , d_{yz} , and d_{z^2} orbitals becomes second lowest in energy for $U > 3.5$ eV (top panel in Fig. 8). The impact of Coulomb interactions on octahedral rotations also gives rise to differences in the response of CTO to changes in U , as compared to STO. For STO, the energies of the in-gap and conduction bands at Γ vary in a manner qualitatively similar to that of CTO, but the orbital character of the bands hardly changes. By contrast, for CTO, within our resolution, the energy at Γ of the lowest conduction state shows only a small variation, but its orbital character significantly evolves from being predominantly d_{xy} to being mainly d_{yz} (bottom panel in Fig. 8). The transfer of weight from the d_{xy} to the d_{yz} component of the wave function

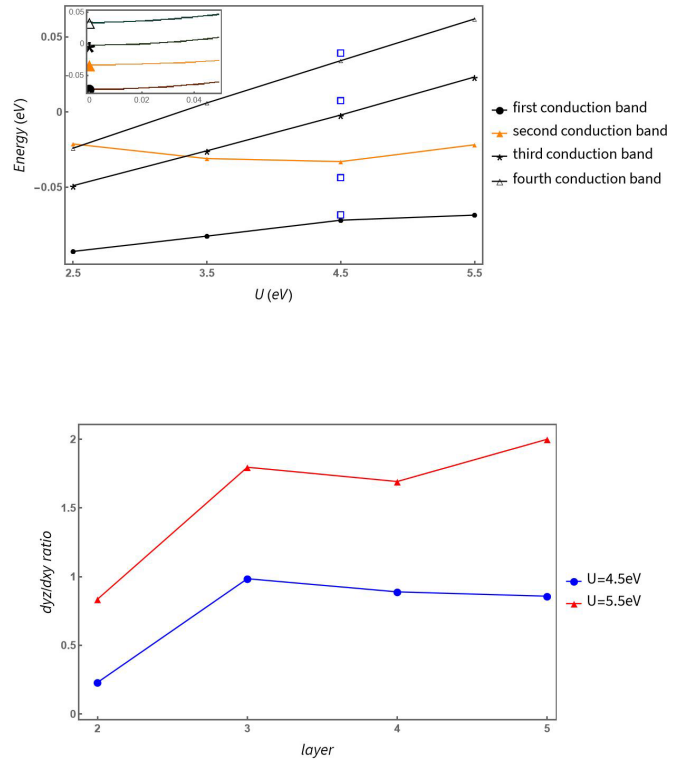


FIG. 8. Top: Evolution of the band energies at Γ . The band ordering for $U = 4.5$ eV is chosen as the reference (shown in the inset). We track the changes in the four lowest band energies with U variations or with a 1% compressive strain when $U = 4.5$ eV (open squares). Bottom: Ratio of the d_{yz} over d_{xy} orbital weight of the first conduction band, for $U = 4.5$ eV and $U = 5.5$ eV; the d_{yz} component of the eigenstate increases when U gets larger.

mitigates the increase in the energy of the band, consistently with Hund rules. Similarly, for the eigenstate combining the three out-of-plane orbitals, a variation in U causes a redistribution of their relative weights with only a minor change in energy (Fig. 8).

The qualitative impact of an in-plane strain may be rationalized. A compressive deformation changes the angles of the Ti-O-Ti bonds, causing a weaker in-plane bonding such that hoppings involving in-plane orbitals get smaller. Conversely, a tensile deformation affects the out-of-plane orbitals' hoppings negatively. This behavior is indeed observed in experiments and DFT calculations on STO where conduction-band states essentially consist of a single orbital component [43,44]. These considerations also pertain to CTO. The top panel in Fig. 8 shows the change in energy at Γ of the lowest conduction bands when our slab is subjected to a one-percent compressive strain with the U value set to 4.5 eV. The energy of the first, third, and fourth bands, which have a dominant d_{xy} character, increases, while the energy of the second band decreases. In addition to the above effect, the expected response to an in-plane compression is a decrease of the tilt and an increase of the rotation [25]. We confirm this evolution when we measure the angles in layer L2. For instance, the tilt angle decreases from 14° to 13° upon applying a 1% strain. This entails that the d_{xy} (d_{yz}) weight of the lowest conduction band gets smaller (larger). We observe this trend since

the fraction of the d_{yz} component in the lowest conduction-band wave function is approximately 20% larger than it is for the stress-free case. For larger values of the deformation, experimental studies of strained CTO thin films reveal the existence of a robust ferroelectric phase [45]. Our *ab initio* results highlight a spatial dichotomy across the slab between a subsurface region where the 2DES is confined and a bulklike region which is insulating and essentially unaffected by the near surface oxygen defects. Under strain, the latter region might host ferroelectricity. Exploring such scenario is beyond the scope of the present work.

IV. SUMMARY AND PERSPECTIVES

When oxygen defects are added to the TiO_2 surface of a CaTiO_3 slab, the main features of the conducting (2DES) states obtained in our *ab initio* calculations (energies, orbital character) fairly match ARPES spectra in the single-vacancy or divacancy cases. Additionally, an in-gap state is found in the divacancy case, but also for other configurations which do not yield a 2DES. Since ARPES probes an area at the surface with a typical ten-micrometer linear size, spectra are averages over many types of impurities. Nevertheless, we focused on the divacancy configuration at the TiO_2 end as it produces both an in-gap state and a 2DES that compare favorably with the experimental data. Rotations and tilts cause all three t_{2g} orbitals to mix and e_g components to contribute to the low-energy states. Compared to SrTiO_3 or BaTiO_3 where such mixing is negligible, confinement is weaker and the carrier mass of the lowest-energy band is larger; this is because the

out-of-plane components of the eigenstates are far less spatially localized than the in-plane ones and have a heavier mass. Between Γ and E_F , the lowest eigenstate involves (dominant) in-plane and (subdominant) out-of-plane t_{2g} orbitals and the second lowest is a combination of out-of-plane orbitals. The effective mass of the lowest conduction band near the origin of the BZ is $\sim 20\%$ smaller than that extracted from the ARPES data, indicating a moderately correlated system. Between Γ and E_F , the energy of the lowest band is only slightly sensitive to changes in U or strain, while that of the second-lowest band increases (decreases) when a compressive (tensile) constraint is applied. The relative weights of the in-plane and out-of-plane components strongly depend on these parameters. Such behavior, which should be contrasted with that reported in DFT studies of strained STO [43], can be linked to the rotations and tilts of the octahedra. In the large filling limit of the d shell, rotational degrees of freedom give promising magnetotransport properties to rare-earth nickelates [46] and strontium iridate (SrIrO_3) [47,48]. This suggests that in the low filling regime, the interplay of rotational and orbital degrees of freedom could similarly endow the CTO 2DES with orbitronic [49] or ferroelectric [45,50] functionalities.

ACKNOWLEDGMENTS

We thank Philippe Ghosez Alexandre Gloter and Marcus Schmitt for insightful discussions. M.G. acknowledges support by a public grant from the French National Research Agency (ANR) as part of the ‘‘Investissements d’Avenir’’ program (Labex NanoSaclay ANR-10-LABX-0035).

-
- [1] A. Soumyanarayanan, N. Reyren, A. Fert, and C. Panagopoulos, *Nature (London)* **539**, 509 (2016).
- [2] Y. Tokura, M. Kawasaki, and N. Nagaosa, *Nat. Phys.* **13**, 1056 (2017).
- [3] Y.-Y. Pai, A. Tylan-Tyler, P. Irvin, and J. Levy, *Rep. Prog. Phys.* **81**, 036503 (2018).
- [4] K. Kormondy, L. Gao, X. Li, S. Lu, A. Posadas, S. Shen, M. Tsoi, M. McCartney, D. Smith, J. Zhou, Leonid Lev *et al.*, *Sci. Rep.* **8**, 7721 (2018).
- [5] A. Gupta, H. Silotia, A. Kumari, M. Dumen, S. Goyal, R. Tomar, N. Wadehra, P. Ayyub, and S. Chakraverty, *Adv. Mater.* **34**, 2106481 (2022).
- [6] R. Di Capua, M. Verma, M. Radovic, V. N. Strocov, C. Piamonteze, E. B. Guedes, N. C. Plumb, Y. Chen, M. D’Antuono, G. M. De Luca *et al.*, *npj Quantum Mater.* **7**, 41 (2022).
- [7] A. Ohtomo and H. Hwang, *Nature (London)* **427**, 423 (2004).
- [8] D. A. Dikin, M. Mehta, C. W. Bark, C. M. Folkman, C. B. Eom, and V. Chandrasekhar, *Phys. Rev. Lett.* **107**, 056802 (2011).
- [9] L. Li, C. Richter, J. Mannhart, and R. Ashoori, *Nat. Phys.* **7**, 762 (2011).
- [10] A. D. Caviglia, M. Gabay, S. Gariglio, N. Reyren, C. Cancellieri, and J.-M. Triscone, *Phys. Rev. Lett.* **104**, 126803 (2010).
- [11] F. Trier, P. Noël, J.-V. Kim, J.-P. Attané, L. Vila, and M. Bibes, *Nat. Rev. Mater.* **7**, 258 (2022).
- [12] K. Yasuda, A. Tsukazaki, R. Yoshimi, K. Kondou, K. S. Takahashi, Y. Otani, M. Kawasaki, and Y. Tokura, *Phys. Rev. Lett.* **119**, 137204 (2017).
- [13] T. C. Rödel, F. Fortuna, S. Sengupta, E. Frantzeskakis, P. L. Fèvre, F. Bertran, B. Mercey, S. Matzen, G. Agnus, T. Maroutian *et al.*, *Adv. Mater.* **28**, 1976 (2016).
- [14] E. Frantzeskakis, T. C. Rödel, F. Fortuna, and A. F. Santander-Syro, *J. Electron Spectrosc. Relat. Phenom.* **219**, 16 (2017).
- [15] S. McKeown Walker, F. Y. Bruno, and F. Baumberger, *Spectroscopy of Complex Oxide Interfaces: Photoemission and Related Spectroscopies*, edited by C. Cancellieri and V. N. Strocov (Springer International, Cham, 2018), pp. 55–85.
- [16] A. Santander-Syro, F. Fortuna, C. Bareille, T. Rödel, G. Landolt, N. Plumb, J. Dil, and M. Radović, *Nat. Mater.* **13**, 1085 (2014).
- [17] T. Taniuchi, Y. Motoyui, K. Morozumi, T. C. Rödel, F. Fortuna, A. F. Santander-Syro, and S. Shin, *Nat. Commun.* **7**, 11781 (2016).
- [18] M. Vivek, M. O. Goerbig, and M. Gabay, *Phys. Rev. B* **95**, 165117 (2017).
- [19] A. Santander-Syro, O. Copie, T. Kondo, F. Fortuna, S. Pailhes, R. Weht, X. Qiu, F. Bertran, A. Nicolaou, A. Taleb-Ibrahimi *et al.*, *Nature (London)* **469**, 189 (2011).
- [20] W. Meevasana, P. D. C. King, R. H. He, S.-K. Mo, M. Hashimoto, A. Tamai, P. Songsirittihigul, F. Baumberger, and Z.-X. Shen, *Nat. Mater.* **10**, 114 (2011).

- [21] T. C. Rödel, M. Vivek, F. Fortuna, P. Le Fèvre, F. Bertran, R. Weht, J. Goniakowski, M. Gabay, and A. F. Santander-Syro, *Phys. Rev. B* **96**, 041121(R) (2017).
- [22] S. Muff, M. Fanciulli, A. P. Weber, N. Pilet, Z. Ristić, Z. Wang, N. C. Plumb, M. Radović, and J. H. Dil, *Appl. Surf. Sci.* **432**, 41 (2018).
- [23] K. Ueda, H. Yanagi, H. Hosono, and H. Kawazoe, *J. Phys.: Condens. Matter* **11**, 3535 (1999).
- [24] A. Krause, W. Weber, D. Pohl, B. Rellinghaus, A. Kersch, and T. Mikolajick, *J. Phys. D* **48**, 415304 (2015).
- [25] J. M. Rondinelli and N. A. Spaldin, *Adv. Mater.* **23**, 3363 (2011).
- [26] R. I. Eglitis and D. Vanderbilt, *Phys. Rev. B* **78**, 155420 (2008).
- [27] R. I. Eglitis and A. I. Popov, *J. Saudi Chem. Soc.* **22**, 459 (2018).
- [28] G. Kresse and J. Furthmüller, *Phys. Rev. B* **54**, 11169 (1996).
- [29] G. Kresse and J. Hafner, *Phys. Rev. B* **47**, 558 (1993).
- [30] P. E. Blöchl, *Phys. Rev. B* **50**, 17953 (1994).
- [31] G. Kresse and D. Joubert, *Phys. Rev. B* **59**, 1758 (1999).
- [32] J. P. Perdew, J. A. Chevary, S. H. Vosko, K. A. Jackson, M. R. Pederson, D. J. Singh, and C. Fiolhais, *Phys. Rev. B* **46**, 6671 (1992).
- [33] S. L. Dudarev, G. A. Botton, S. Y. Savrasov, C. J. Humphreys, and A. P. Sutton, *Phys. Rev. B* **57**, 1505 (1998).
- [34] J. Shen, H. Lee, R. Valenti, and H. O. Jeschke, *Phys. Rev. B* **86**, 195119 (2012).
- [35] H. O. Jeschke, J. Shen, and R. Valenti, *New J. Phys.* **17**, 023034 (2015).
- [36] H. J. Monkhorst and J. D. Pack, *Phys. Rev. B* **13**, 5188 (1976).
- [37] J. Padilla and D. Vanderbilt, *Phys. Rev. B* **56**, 1625 (1997).
- [38] J. Padilla and D. Vanderbilt, *Surf. Sci.* **418**, 64 (1998).
- [39] M. Altmeyer, H. O. Jeschke, O. Hijano-Cubelos, C. Martins, F. Lechermann, K. Koepf, A. F. Santander-Syro, M. J. Rozenberg, R. Valenti, and M. Gabay, *Phys. Rev. Lett.* **116**, 157203 (2016).
- [40] T. Mizokawa and A. Fujimori, *Phys. Rev. B* **51**, 12880 (1995).
- [41] A. Marthinsen, T. Grande, and S. M. Selbach, *J. Phys. Chem. C* **124**, 12922 (2020).
- [42] C. Ricca, I. Timrov, M. Cococcioni, N. Marzari, and U. Aschauer, *Phys. Rev. Res.* **2**, 023313 (2020).
- [43] A. Janotti, D. Steiauf, and C. G. Van de Walle, *Phys. Rev. B* **84**, 201304(R) (2011).
- [44] E. Bonini Guedes, T. Willemoes Jensen, M. Naamneh, A. Chikina, R. T. Dahm, S. Yun, F. M. Chiabrera, N. C. Plumb, J. H. Dil, M. Shi *et al.*, *J. Vacuum Sci. Technol. A* **40**, 013213 (2022).
- [45] R. C. Haislmaier, Y. Lu, J. Lapano, H. Zhou, N. Alem, S. B. Sinnott, R. Engel-Herbert, and V. Gopalan, *APL Mater.* **7**, 051104 (2019).
- [46] S. Catalano, M. Gibert, J. Fowlie, J. Iniguez, J.-M. Triscone, and J. Kreisel, *Rep. Prog. Phys.* **81**, 046501 (2018).
- [47] J.-M. Carter, V. V. Shankar, M. A. Zeb, and H.-Y. Kee, *Phys. Rev. B* **85**, 115105 (2012).
- [48] Y. F. Nie, P. D. C. King, C. H. Kim, M. Uchida, H. I. Wei, B. D. Faeth, J. P. Ruf, J. P. C. Ruff, L. Xie, X. Pan *et al.*, *Phys. Rev. Lett.* **114**, 016401 (2015).
- [49] H. Wang, Y.-X. Huang, H. Liu, X. Feng, J. Zhu, W. Wu, C. Xiao, and S. A. Yang, Theory of intrinsic in-plane Hall effect (unpublished).
- [50] C.-J. Eklund, C. J. Fennie, and K. M. Rabe, *Phys. Rev. B* **79**, 220101(R) (2009).